

3D Gaussian Splatting for Large-scale 3D Surface Reconstruction from Aerial Images

YuanZheng Wu, Jin Liu, Shunping Ji

Abstract—Recently, 3D Gaussian Splatting (3DGS) has garnered significant attention. However, the unstructured nature of 3DGS poses challenges for large-scale surface reconstruction from aerial images. To address this gap, we propose the first large-scale surface reconstruction method for multi-view stereo (MVS) aerial images based on 3DGS, named **Aerial Gaussian Splatting (AGS)**. Initially, we introduce a data chunking method tailored for large-scale aerial imagery, making the modern 3DGS technology feasible for surface reconstruction over extensive scenes. Additionally, we integrate the Ray-Gaussian Intersection method to obtain normal and depth information, facilitating geometric constraints. Finally, we introduce a multi-view geometric consistency constraint to enhance global geometric consistency and improve reconstruction accuracy. Our experiments on multiple datasets demonstrate for the first time that the GS-based technique can match traditional aerial MVS methods on geometric accuracy and beat state-of-the-art GS-based methods on geometry and rendering quality.

Index Terms—3D Gaussian splatting, Oblique photography

I. INTRODUCTION

THE reconstruction of large-scale 3D scenes has long been a focal point of interest in both academic research and industrial applications, particularly in domains such as aerial surveying [20] and smart city development [3] [2]. Recently, NeRF-based methods [21] [22] [19] have been extensively researched in image rendering, especially for foreground targets. Besides, they have also the potential ability for geometric reconstruction [27] [12]. However, the intensive computational demands of volumetric rendering in NeRF-based approaches result in extended training times, often spanning several hundred hours or even unaffordable, thus real-time rendering and accurate 3D reconstruction remain a significant challenge in large-scale scenarios. The emergence of the 3D Gaussian Splatting(3DGS) technology offers a solution to these limitations. In contrast to NeRF-based methods, 3D Gaussian Splatting uses explicit 3D Gaussians instead of implicit Multi-Layer Perceptions (MLPs) to represent entire scenes. The rendering process is accomplished by optimizing parameters such as positions, rotations, and scales of a Gaussian primitive. 3DGS markedly reduces computational requirements and enables more efficient scene reconstruction and rendering. thus benefiting large-scale reconstruction from aerial images acquired from planes or unmanned aerial vehicles (UAVs).

Although 3DGS has demonstrated high-fidelity novel view generation and real-time rendering capabilities, it remains a significant challenge to achieve large-scale aerial surface reconstruction with a geometric precision that matches or surpasses conventional or deep learning-based multi-view stereo

(MVS) methods. Firstly, the extensive scenes and a large number of aerial images impose substantial computational demands. This often leads to out-of-memory issues on a modern GPU. Moreover, the inherent limitations of 3D Gaussian primitives in accurately capturing depth and normal vectors make it difficult to apply 3DGS directly to surface reconstruction tasks, typically resulting in low-precision surface models. Moreover, the original 3D Gaussian Splatting approach relies solely on image loss for optimization, which skews the Gaussian distribution toward high-fidelity image rendering at the expense of surface geometry accuracy. To address these challenges and achieve high-quality surface geometric reconstruction of large aerial scenes, we propose a novel framework based on 3DGS for large-scale 3D surface reconstruction from aerial images. This is the first time 3DGS methods have been applied to aerial imagery to realize high-precision surface reconstruction.

The proposed large-scale surface reconstruction framework, named **Aerial Gaussian Splatting (AGS)**, uses 3DGS [10] as our baseline. However, this vanilla method cannot handle large-scale scenarios due to high memory demands. Therefore, our first contribution in this work is to adapt 3DGS to large-scale aerial scenes. we apply a new chunking method to partition the whole scene into multiple blocks and independently optimize each data block, then reassemble them to form a complete scene, termed **Adaptive Aerial Image Scene Partitioning**. A major challenge in aerial scene partitioning is the uneven distribution of point clouds—sparse areas lack sufficient views for effective optimization, while dense areas often suffer from redundant views. To mitigate this issue, we divide the scene into multiple blocks based on camera positions, ensuring each region contains a consistent number of views. Additionally, to address the floating artifacts and noise typically found at the edges of scenes in 3DGS methods, we extend the boundaries of each region and incorporate all point clouds within each extended region. Subsequently, we introduce an innovative viewpoint selection and culling strategy that effectively removes unsuitable viewpoints from the data block and supplements them with additional key viewpoints, ensuring that each data block is fully optimized. Finally, we incorporate point clouds visible in these N views into the data block as initial points for optimization. This chunking method, specifically tailored for large-scale aerial imagery, effectively improves both geometric accuracy and rendering quality.

If we directly use 3DGS primitives for surface reconstruction, the inherent spherical nature of 3D Gaussian primitives makes it challenging to extract precise depth and normal

vector information for each primitive. This limitation hinders the ability to apply effective geometric constraints. To overcome this issue, the proposed method adopts the idea from [11] [32]. This approach, known as the Ray-Gaussian Intersection, is capable of obtaining accurate depth and normal vector information. When the precise depth and normal vector information are obtained, we impose depth and normal consistency constraints. Furthermore, to reduce floating artifacts and improve global geometric consistency, as with some MVS methods [15], we introduce a global geometric consistency strategy. This method calculates the error of the rendered depth maps through projection and incorporates error into the loss function. By doing so, we improve the reconstruction of surface details, resulting in higher-quality surface reconstruction and more accurate geometric alignment across the partitioned regions.

We evaluated the geometric accuracy of our framework on the WHU-OMVS. The experimental results show that the proposed method outperforms the 3DGS-based approach and, in some cases, even surpasses the open-source MVS software COLMAP [23] [24] and OpenMVS. Additionally, we validated the rendering quality of the proposed method on scenes in the Mill-19 [26] and UrbanScene3D [14] datasets, where the results achieved a highly competitive level. Our contributions are summarized as follows:

- We introduce, for the first time, a large-scale aerial surface reconstruction and rendering method based on 3D Gaussian Splatting.
- We adapt 3DGS to large scenes by designing a new scene chunking method that effectively segments scene point clouds and viewpoints in large-scale environments.
- We introduce a multi-view geometric consistency constraint and the Ray-Gaussian Intersection strategy into the framework, which significantly improved geometric accuracy.
- We conducted experiments on multiple datasets, and the results demonstrate that the proposed method achieves high-quality geometric reconstruction and delivers high-fidelity rendering.

II. RELATED WORK

A. Novel View Synthesis

Novel View Synthesis (NVS) has gained significant attention from both academia and industry. Neural Radiance Fields (NeRF) [21] have notably impacted the NVS domain by using MLPs to model scenes with 5D input (spatial, position and direction). It achieves high-fidelity scene representation by predicting density and color from 5D input. However, the high computational demands and time required for both training and rendering make it challenging to deploy in real-time or large-scale scenarios. To reduce NeRF's computational demands, Plenoxels [4] uses 3D sparse grids to represent scene points, which decreases computational complexity and storage requirements and also enhances speed compared to vanilla NeRF. However, the use of voxel grids in Plenoxels leads to a degradation of fine details. Efforts like Mip-NeRF

[1] and Tri-MipRF [8] enhance rendering quality with multi-scale representations and anti-aliasing, improving quality without sacrificing efficiency.

Recently, 3D Gaussian Splatting [10] has gained attention for its ability to achieve high-fidelity and real-time rendering. Follow-up work, such as Mip-Splatting [31], employs 3D smoothing filters to improve rendering quality. Scaffold-GS [18] advances this by utilizing anchor points to distribute local 3D Gaussian distributions, enabling real-time adjustment of Gaussian distribution and density to meet the specific needs of the scene.

B. Surface Reconstruction

Early methods for 3D surface reconstruction require significant manual intervention and offer low automation. Over the decades, image-based reconstruction has advanced considerably. Methods like COLMAP [23] [24] or OpenMVS use Structure from Motion (SfM) to estimate camera poses and generate sparse point clouds, and then apply Multi-View Stereo (MVS) techniques to create dense point clouds or triangulated meshes. Except for conventional MVS methods like SGM [7], learning-based MVS methods [30] [16] have also been explored with the rapid development of deep learning, and some of them are embedded into a whole framework for scene reconstruction [14].

Recently, some works have attempted to apply NeRF or Gaussian-based methods, which have shown exceptional performance in novel view synthesis tasks to surface geometric reconstruction. NeuS [27] combines the strengths of both volumetric and surface rendering by optimizing a continuous Signed Distance Functions (SDF) and color field to reconstruct fine surface details, but it requires substantial computational resources and inference time. Neuralangelo [12] improves 3D surface reconstruction fidelity by combining multi-resolution 3D hash grids with neural surface rendering. However, it remains constrained by computational resource demands.

The emergence of 3D Gaussian Splatting [10] has introduced new approaches for surface reconstruction. SuGaR [6] compresses 3D Gaussian spheres into approximate 2D ellipses during training and uses Poisson reconstruction to extract a continuous mesh from 3D point clouds, which were sampled using the density field from the Gaussian. However, the lack of geometric constraints results in dispersed point clouds and meshes with many holes. 2D Gaussian Splatting [9] replaces 3D Gaussians with 2D disks, addressing the limitations of vanilla 3DGS in geometric reconstruction. However, 2D GS still encounters challenges in capturing the full details of large-scale scenes.

Currently, GS-based methods predominantly focus on close-range natural scene, and large-scale surface reconstruction remains unexplored largely.

C. Large Scene Reconstruction

With the advancement of radiance field technology, its application has expanded from close-range objects to larger-scale scenes. Block-NeRF [25] and Mega-NeRF [26] used data chunking strategies to handle large-scale scene generation,

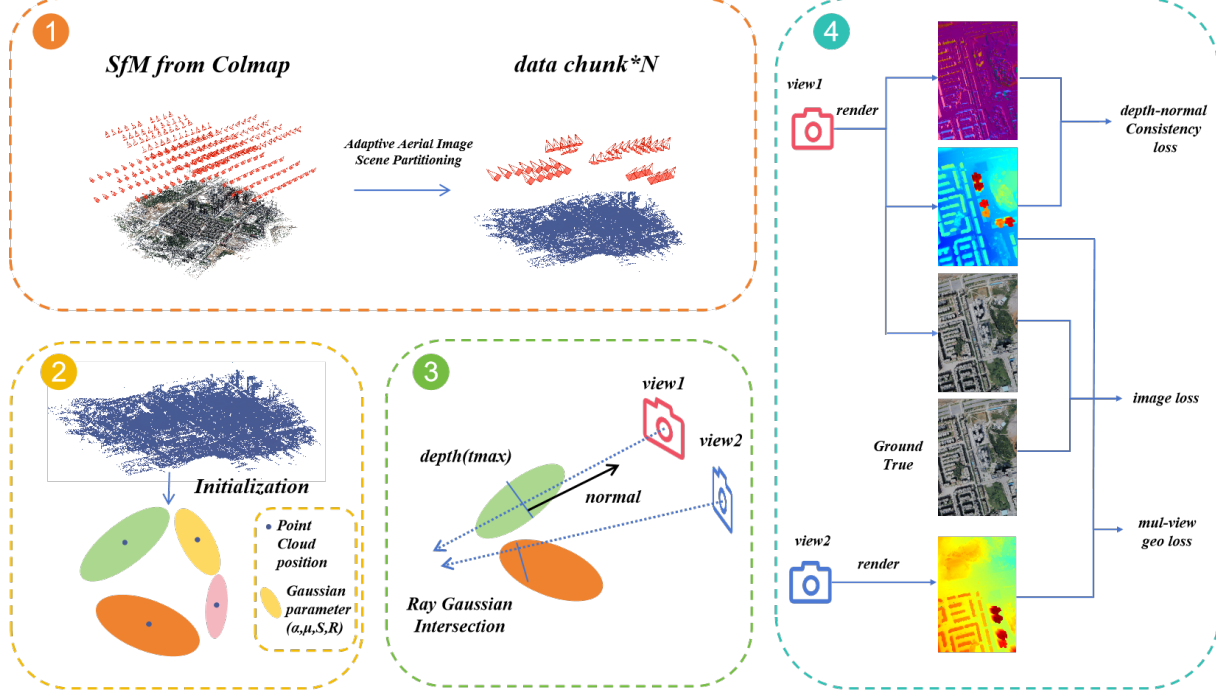


Fig. 1. The overview of Aerial 3D Gaussian Splatting Framework.(1)The SfM sparse point cloud and views are divided into N data blocks.(2) The point clouds in each block used to initialize the 3D Gaussians.(3) The Ray-Gaussian Intersection technique provides reliable depth and normal vector information.(4)The depth map and normal map are utilized to compute the depth-normal consistency loss and multi-view geometric consistency loss.

while UE4-NeRF [5] combined NeRF with Unreal Engine 4 for scalable rendering and scene editing. Switch-NeRF [33] used a mixture of expert models for scene decomposition, enhancing large-scale reconstruction.

Although 3DGS has gained attention for its quick training and high-fidelity rendering, there is still a noticeable gap in the research when it comes to large-scale aerial imagery. Applications like CityGaussian [17] have explored large-scale scene rendering using chunking and level of Detail (LOD) methods, addressing challenges to rendering efficiency and scalability. Similarly, VastGaussian [13] addresses lighting effects on rendering, further refining the visual quality of large-scale scenes. However, these large-scale methods with NeRF and 3D Gaussian Splatting remain focused primarily on image rendering. Our work seeks to extend these techniques to surface reconstruction from large-scale aerial MVS images. We propose a novel scene chunking method, introduce Ray-Gaussian Intersection to provide precise depth and normal vectors for geometric constraints and add a global consistency loss to ensure overall geometric consistency, enhancing the ability of proposed method to capture fine details in large-scale scene reconstruction.

III. PRELIMINARIES

3D Gaussian Splatting(3DGS) [10] represents scenes explicitly using a large number of 3D Gaussian primitives(ellipsoids).Each Gaussian primitive is characterized by four key parameters that require optimization: position, covariance, opacity and spherical harmonics (SH) coefficients. Using these four parameters, α -blending algorithm is employed to render a new image from these 3D gaussians. Specifically, for

a pixel in the rendered image, the color of can be obtained by:

$$C = \sum_{i \in N} \alpha_i c_i \prod_{j=1}^{i-1} (1 - \alpha_j) \quad (1)$$

where N represents the set of all Gaussians, c_i is the view-dependent color of the i -th Gaussian, derived from spherical harmonics coefficients, α_i is determined by the GS distribution and the Gaussian's opacity σ_i , as seen in Equation (2).

$$\alpha_i = \sigma_i \exp\left(-\frac{1}{2}(p - \mu_i)^T \Sigma_i^{-1} (p - \mu_i)\right) \quad (2)$$

The parameters Σ is given by $\Sigma = RSS^T R^T$, where $R \in \mathbb{R}^{3 \times 3}$ is the rotation matrix and $S \in \mathbb{S}^{3 \times 1}$ is the scale matrix. μ_i represents the location of the GS primitive.

IV. METHOD

A 3DGS-based surface reconstruction framework tailored for aerial multi-view images is introduced, named Aerial 3D Gaussian Splatting (AGS). In contrast to the original 3DGS [10], the proposed method incorporates several innovative and necessary modules. Specifically, we introduce Adaptive Aerial Image Scene Partitioning to effectively segment large-scale scenes and guarantee optimal merging at the final step. Furthermore, the Ray-Gaussian Intersection technique is employed to address deficiencies of 3D gaussian in surface geometric reconstruction. Finally, a global geometric consistency loss is incorporated to enforce global geometric coherence across the reconstructed surfaces. The framework is shown in Fig.1

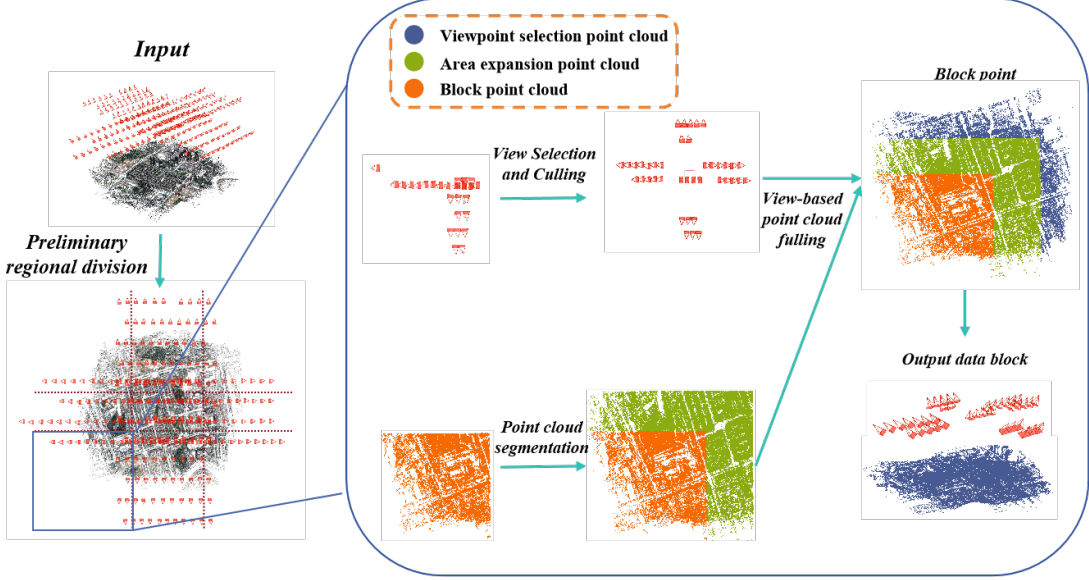


Fig. 2. Overview of Adaptive Aerial Image Scene Partitioning strategy. Our chunking method first divides the entire scene into N regions based on camera positions, as illustrated by the example of 9 regions in the figure. These regions are then expanded at their boundaries, and viewpoints (i.e., cameras) are selected and culling. Finally, all points visible from the selected viewpoints in each data block are added to the block's point cloud.

A. Adaptive Aerial Image Scene Partitioning

Inspired by Vast-Gaussian [13], the target scene is divided into multiple data blocks, each comprising point cloud and corresponding camera views. To ensure that each data block contains sufficient and correctly oriented data for optimization, we design a new Adaptive Aerial Image Scene Partitioning strategy, which consists of four steps. The pipeline of Adaptive Aerial Image Scene Partitioning is shown in Fig.2.

Preliminary regional division: The naive scene partitioning method typically involves dividing the target scene into uniform blocks based on the positions of point clouds. However, in the city-level scene covered by multiply aerial images, the distribution of point cloud, which is processed through Structure from Motion (SfM), is often uneven—some areas have sparse point clouds, while others are densely populated. This uneven distribution can result in an imbalance of viewpoints across different blocks, with some blocks having an excessive number of viewpoints while others lacking sufficient coverage. To address this issue, following Vast-Gaussian, a segmentation method based on camera positions is proposed. For a scene divided into $M \times N$ blocks with n viewpoints, we first horizontally divide the cameras into M blocks, with each block containing n/M cameras. Then, we further divide the M blocks vertically, with each block containing $\frac{n}{M \times N}$ viewpoints.

Point cloud segmentation: Following the initial regional division, point clouds within each respective region are aggregated to form point cloud blocks. However, in typically optimized scenes, objects at the center of the scene tend to receive sufficient optimization, whereas objects near the boundaries may suffer from artifacts due to insufficient optimization information. To reduce these artifacts across the entire scene, we extend each region by a certain proportion, ensuring that each scene block is adequately optimized.

View selection and culling: Given that we have expanded the boundaries of each data block to include point clouds, it is necessary to incorporate supplementary viewpoints to enhance the scene optimization. Therefore, we design a viewpoint selection and culling strategy. This strategy involves projecting all point clouds within a data chunk onto all images and calculating projection scores to determine the suitability of each viewpoint.

$$region = \begin{cases} H * scale \leq p_y \leq H - H * scale \\ W * scale \leq p_x \leq W - W * scale \end{cases} \quad (3)$$

$$score = \begin{cases} 1 & \text{if } p \text{ in region} \\ 0 & \text{else} \end{cases} \quad (4)$$

As shown in the equation, H and W represent the height and width of the image, p denotes the pixel coordinates of the projected point, $region$ refers to the region used for aggregating the projection statistics. The projection score is determined by counting the number of point clouds projected onto an image, with calculations focused on points projected onto the central area of the images. Subsequently, all images are sorted based on their projection scores. For each region, the top N images are selected as viewpoints to optimize the regional scene. This selection strategy not only filters out unsuitable viewpoints but also supplements the block with essential viewpoints for comprehensive optimization.

View-based point cloud fulling: In the previous step, we supplemented the data block with some new viewpoints. To ensure that there are enough points in the scene for initialization and to reduce the impact of artifacts, we incorporated the sparse point cloud results from the SfM of all new viewpoints into the data block.

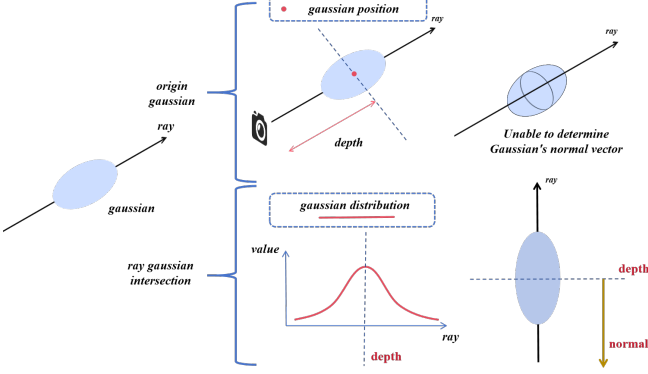


Fig. 3. Ray-Gaussian Intersection. By calculating the maximum Gaussian value along the ray, we can obtain accurate depth and normal vector information for the Gaussian.

B. Ray-Gaussian Intersection

Ray-Gaussian Intersection: Original 3D Gaussian Splatting projects 3D Gaussians into 2D screen space for rendering, merely using the distance of each Gaussian sphere to the screen as depth and lacking normal vector information. However, in surface reconstruction tasks, reliable depth information and normal vector data are essential for geometric constraints. To address these issues, we introduce the Ray-Gaussian Intersection technique to improving the accuracy of geometric reconstruction. Specially, an arbitrary point along the ray is defined as $x = o + tr$, with o being the camera center, r the ray direction, and t the depth of r . Next, o, r is converted to the gaussian local coordinate system o_g, r_g . point x in the local coordinate system of the Gaussian is $x_g = o_g + tr_g$. After the coordinate system transformation, we can reduce the Gaussian function from 3D to 1D:

$$g_k^{1D}(t) = e^{-\frac{1}{2}x_g^T x_g} \quad (5)$$

Thereby, the depth value corresponding to the maximum Gaussian value can be computed as:

$$t_{max} = \frac{(\mu - r_o)^T \Sigma r_d}{r_d^T \Sigma r_d} \quad (6)$$

After obtaining the depth value, the Gaussian's normal is derived as the normal to the intersection plane perpendicular to the given ray direction. For image rendering, the same α -blending algorithm as in 3D Gaussian Splatting (3DGS) is employed to compute pixel colors.

Depth-Normal Consistency Constraints: After obtaining the depth and normal vector information, the relevant geometric constraints can be enforced. Specifically, this involves calculating the error between the normal map and the gradient values of the depth map as the loss function:

$$L_n = \sum_i \omega_i (1 - n_i^T N) \quad (7)$$

Here, i represents the gaussian index, and ω_i denotes the blending weight. n_i represents the normal vector of the Gaussian, and N is the normal vector calculated from the depth map. The normal vector at point p is computed as Eq.(8), in

which p represents the pixel coordinates, and ∇ represents the gradient value.

$$N(x, y) = \frac{\nabla_x p \times \nabla_y p}{\nabla_x p \cdot \nabla_y p} \quad (8)$$

C. Global geometric consistency loss

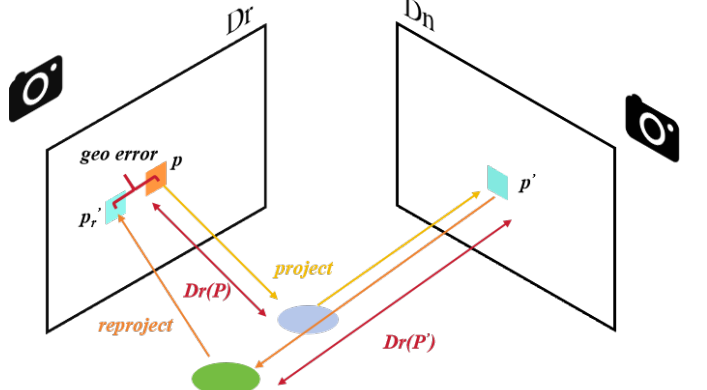


Fig. 4. Global geometric consistency constraints. The multi-view geometric consistency constraints are modelled as the error between projection and reprojection.

In previous methods, geometric constraints predominantly enforced on a single viewpoint. For example, in 2D Gaussian Splatting [9], the consistency between the normal map and depth normal map was utilized to enforce geometric coherence. However, such single-view loss often led to overfitting to specific images, thereby compromising global geometric consistency and diminishing overall reconstruction accuracy. To address this issue, we introduce a global geometric consistency constraint to ensure global geometric coherence across multiple views.

As shown in Fig.4, we render the depth maps for two adjacent viewpoints V_r and V_n , denoted as D_r and D_n . Firstly, a pixel P in the reference view V_r is projected onto the adjacent view V_n through its rendering depth value $Dr(P)$ and the intrinsic and extrinsic parameters, yielding the projected point P' in V_n . Subsequently, the projected point P' is reprojected onto the reference view based on its rendering depth value $Dn(P')$, resulting in the reprojected pixel P'_r . The distance between the coordinate of P and P'_r is calculated as the geometric consistency loss:

$$L_{geo} = \frac{1}{V} \sum_{P \in V} \|P - P'_r\| \quad (9)$$

However, during the projection and reprojection processes, significant occlusions between viewpoints can lead to significant deviations in the calculation of pixel distances. To mitigate the influence of such outliers, a threshold T (It is usually set to 1) is employed to exclude these anomalies, with distance exceeding T being set to zero. When computing the loss, only the non-zero values are averaged, as indicated in Eq.(9), where V represents the valid pixels.

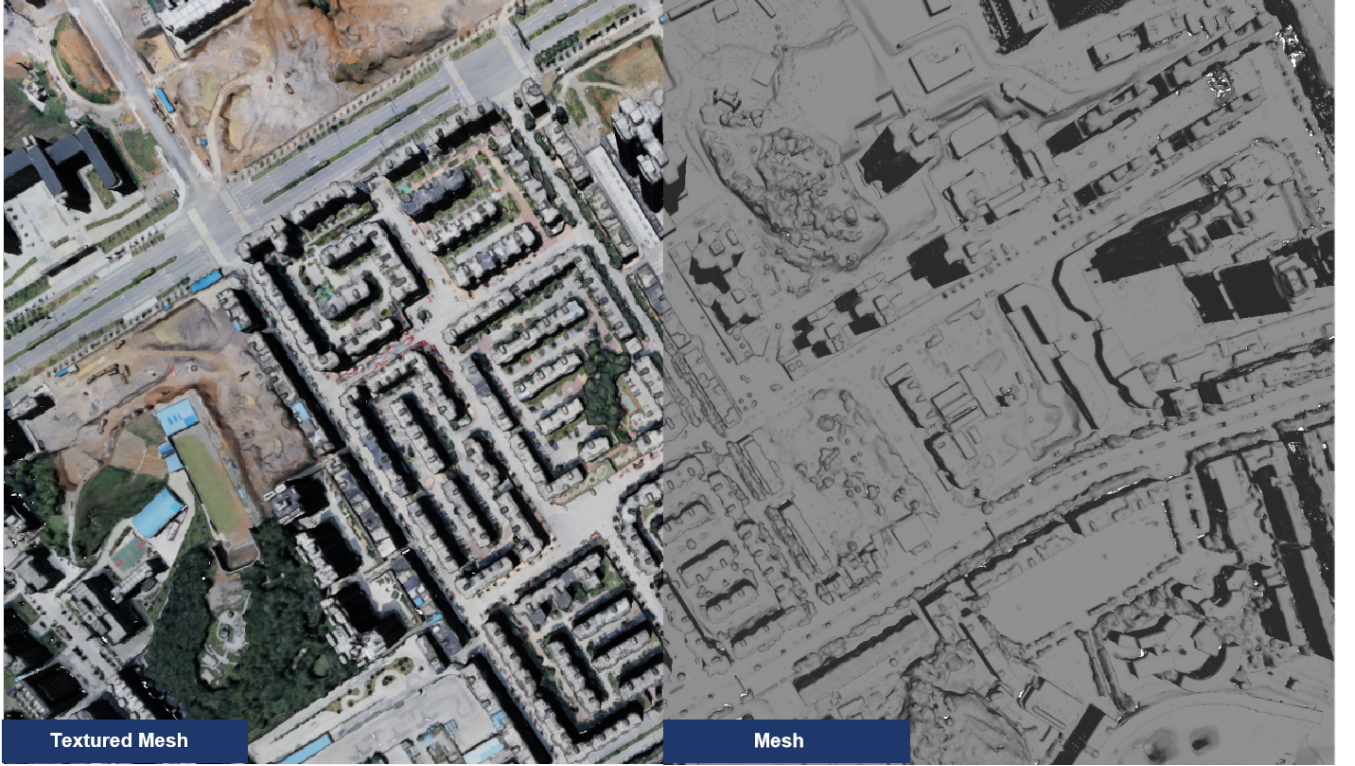


Fig. 5. Surface reconstruction results of WHU-OMVS dataset

D. Seamless Merging

After optimizing each data block, all blocks are subsequently merged to form a coherent scene. This is achieved by removing the expanded regions of each block before merging. After this, all data blocks are merged seamlessly according to their original regions without any additional adjustments.

V. EXPERIMENT

A. Implementation

When evaluating the proposed method, we first perform Manhattan alignment on the target scene, aligning the y-axis to be perpendicular to the ground to facilitate the chunking process. Each block is expanded by 20%. During training, each data block is independently optimized for 50,000 iterations. Densify begins after 500 iterations and ends at 30,000 iterations. We introduce the global geometric consistency loss and depth-normal consistency constraint at 7,000 iterations. And the other settings remain consistent with those used in the original 3D Gaussian Splatting (3DGS) method [10]. All the experiments were performed on NVIDIA RTX 4090 GPU. We used the SfM module in Colmap [24] [23] to obtain the sparse point cloud. Following the 2D Gaussian Splatting [9] approach, we used TSDF [28] for surface reconstruction.

B. Dataset

WHU-OMVS: This dataset covers an area of Guizhou, China, with a ground resolution of 10 cm. Images are captured from a camera rig with one nadir and four oblique viewpoints, with a total number of 268 and each has size of 3712×5504

pixels. The flight height is 550 meters, covering an area of 850×700 meters. During the training of all methods, we performed a 4x downsampling on the images as in previous studies [17] for rendering and reconstruction due to the limitation of GPU capacity. We take the depth map as the ground truth, and evaluate the geometric accuracy of proposed method on the rendering depth map.

Mill-19 and UrbanScene3D: We applied the proposed method to three open-source large-scale scenes: Rubble and Building from the Mill-19 dataset [26] and Residence from the UrbanScene3D dataset [14], each containing 1,678, 1,940, and 2,582 images. Follow previous rendering methods [17], we performed 4x downsampling operation to the input image during training.

C. Metrics

1) *Surface reconstruction:* Following the work [15], we used the MAE, RMSE, and PAG metrics to evaluate the rendering depth map. The specific explanations of these metrics are as follows:

Mean Absolute Error (MAE): MAE measures the absolute difference between the predicted values and the ground truth, which is calculated by:

$$MAE = \frac{1}{m} \sum_{i=1}^m |y_i - \hat{y}_i| \quad (10)$$

where y_i represents the ground truth value, \hat{y}_i represents the estimated value and m denotes the number of valid values. In our experiments, difference larger than 10 meters are considered as invalid and excluded from the calculation.

TABLE I

THE QUANTITATIVE RESULTS OF SURFACE RECONSTRUCTION ON THE WHU_OMVS DATASET. THE BEST RESULTS ARE HIGHLIGHTED IN **BOLD**.

method	PAG0.6m(%)	PAG0.8m(%)	PAG1.0m(%)	MAE(m)	RMSE(m)
OpenMVS	71.91	77.81	81.18	0.520	1.041
Colmap	71.32	77.44	81.36	0.623	1.287
GOF	79.80	83.83	86.03	0.476	1.155
3DGS*	65.01	73.09	74.98	0.825	1.481
2DGS	56.88	65.57	69.42	0.906	1.483
proposed	81.29	86.13	88.78	0.467	1.019

* Due to the large scale of this dataset, 3D Gaussian methods could not complete the training, resulting in out-of-memory (OOM) errors. We implemented specific parameter adjustments to ensure the method could run properly.



Fig. 6. Qualitative comparisons with different methods. image represents the original image from the viewpoint, while the three images on the right depict the error maps between the predicted depth values and the ground truth. The bands in the error maps indicate the magnitude of the errors, with darker colors representing larger errors.

Root Mean Square Error (RMSE): RMSE calculates the standard deviation of the differences between the estimated values and the ground truth values:

$$RMSE = \sqrt{\frac{1}{m} \sum_{i=1}^m (y_i - \hat{y}_i)^2} \quad (11)$$

Similarly, any errors exceeding 10 meters are treated as invalid and excluded from the computation.

Percentage of Accurate Grids (PAG): PAG measures the proportion of grids with absolute difference below a given threshold α relative to the total number of grids. Three different thresholds: 0.6m, 0.8m and 1m.

$$PAG_\alpha = \left(\frac{m_\alpha}{m} \cdot 100\% \right) \quad (12)$$

m_α represents the valid grid, and m represents the number of all grids.

These metrics provide a comprehensive assessment of the accuracy and performance of the proposed method across different scenarios and resolutions.

2) Image Rendering: Following the work of [26] [33] [17], we use the peak signal-to-noise ratio (PSNR), structural similarity index measure (SSIM), and the learned perceptual image patch similarity (LPIPS) metrics to evaluate the quality of rendering image.

D. Comparison

To validate the reconstruction quality of the proposed method, we conducted surface reconstruction experiments on the WHU-OMVS dataset. Given the limited number of 3DGS-based surface reconstruction methods capable of handling large-scale scenes with significant depth variation, we selected three 3DGS-based methods for comparison: 2D Gaussian Splatting [9], 3D Gaussian Splatting [10], and GOF [32].

TABLE II

THE IMAGE QUALITY OF NOVEL VIEW SYNTHESIS (NVS) ON THE WHU-OMVS DATASET WAS COMPROMISED. THE BEST RESULTS ARE HIGHLIGHTED IN **BOLD**.

method	SSIM↑	PSNR↑	LPIPS↓
GOF	0.925	29.071	0.0666
3DGS*	0.940	31.145	0.0514
2DGS	0.927	29.892	0.0668
proposed	0.939	30.462	0.0270

* Due to the high computational resource demands of 3D Gaussian Splatting in this scene, the training could not be completed. We implemented specific parameter adjustments to ensure the method could run properly.

Besides, we included comparisons with the widely recognized open-source MVS software Colmap [24] [23] and OpenMVS. In addition to surface reconstruction, we also evaluated the rendering quality of the proposed method. We selected several state-of-the-art (SOTA) methods for large-scale rendering: Mega-NeRF [26], Switch-NeRF [33], GridNeRF [29], and CityGaussian [17], and conducted comparative experiments on the Mill-19 [26] and UrbanScene3D [14] datasets.

1) Experimental Results on WHU-OMVS:

Surface reconstruction: The surface reconstruction results on the WHU-OMVS dataset are presented in Table i. The experimental results demonstrate that the proposed method achieves the best reconstruction results at PAG, MAE and RMSE metrics. In the highest-resolution, the proposed method surpassed the second-best GOF by 1.5% and the open-source software Colmap by 9.4%, indicating the proposed method excels in detail reconstruction. In the $PAG_{0.8m}$ and $PAG_{1.0m}$ metrics, the proposed method also outperforms other approaches by large margins. This confirms that the overall reconstruction quality of the proposed method is significantly higher than that of other methods. The depth error distribution of different methods shown in Fig.6 further supports this conclusion. For example, the 2D Gaussian Splatting creates some severe reconstruction errors. Colmap produces large errors at object edges and noticeable holes in some areas. In contrast, the proposed method exhibits smaller overall errors and performs exceptionally well in detailed areas.

Novel View Synthesis: We validate the rendering quality of the proposed method on the WHU-OMVS dataset, as shown in Table ii. The results show that the proposed method significantly outperforms others in LPIPS metric, with approximately a 46% improvement over 3DGS. This indicates that the proposed method achieves excellent visual consistency with the ground truth images. Due to the use of lighting compensation in the proposed method, which causes changes in image brightness, our PSNR score is slightly lower than that of 3D Gaussian Splatting, though it remains competitive. Additionally, Our SSIM score is also very competitive, only 0.001 lower than the best method, indicating that the proposed method excels in structural similarity.

2) Experimental Results on Mill-19 and Urbanscene3d:

To further validate the rendering quality of the proposed method, following the work of [26] [33] [17], we conducted experiments on the Mill-19 and UrbanScene3D datasets. As shown in Table iii, in the Building and Rubble datasets, the proposed method achieves the highest scores across all three

metrics, with PSNR significantly surpassing other methods. This demonstrates that the proposed method delivers optimal perceptual quality, achieving high-fidelity rendering. In the Residence dataset, the proposed method achieves the best results in PSNR and LPIPS. Our SSIM score was slightly lower than that of CityGaussian, but significantly exceeds other methods. Therefore, we can conclude that the proposed method not only excels in high-precision surface reconstruction but also achieves high-fidelity image rendering.

E. Ablation

We conducted ablation experiments mainly on the WHU-OMVS dataset.

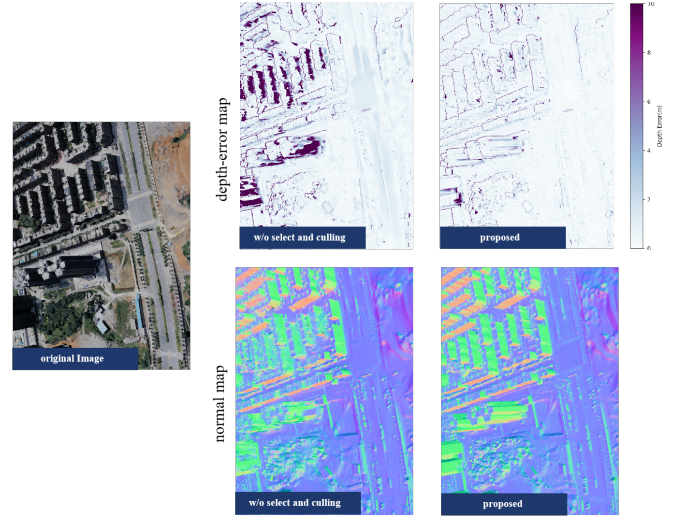


Fig. 7. Comparison with and without Multi-View Geometric Consistency. The comparison reveals that the proposed method, which includes multi-view geometric consistency, provides better detail recovery compared to the version without it.

Viewpoint Selection and Culling: As shown in Table iv, when viewpoint selection and culling are disabled, the proposed method's reconstruction accuracy significantly decreases. This decline is primarily due to insufficient optimized viewpoints and the inclusion of improper viewpoints. As depicted in Fig.7, the absence of proper viewpoints leads to severe errors in local areas of the depth error map, and in the normal map, parts of the buildings appear transparent and unoptimized. Therefore, viewpoint Selection and culling are essential components of the chunking strategy.

Ray-Gaussian Interaction: As shown in Table v, the Ray-Gaussian Interaction significantly improved the performance of proposed method, evidenced by a 12.13% improvement in $PAG_{0.6m}$. This improvement is principally attributable to the Ray-Gaussian Interaction, which provide accurate depth and normal vector information. The utilization of depth and normal information facilitates the imposition of geometric constraints, thereby effectively mitigating the challenges associated with surface reconstruction, particularly those arising from the irregular distribution of Gaussian primitives inherent in the original 3DGS method.

Multi-View Geometric Consistency loss: 3DGS [10] applies losses within single view, which can lead to overfitting

TABLE III
QUANTITATIVE COMPARISON OF RENDERING IMAGE ON THREE DATASETS. THE BEST RESULTS ARE HIGHLIGHTED IN BOLD.

method	residence			Building			Rubble		
	SSIM↑	PSNR↑	LPIPS↓	SSIM↑	PSNR↑	LPIPS↓	SSIM↑	PSNR↑	LPIPS↓
MegaNeRF	0.628	22.08	0.489	0.569	21.48	0.378	0.553	24.06	0.516
Switch-NeRF	0.654	22.57	0.457	0.594	22.07	0.332	0.562	24.31	0.496
GP-NeRF	0.661	22.31	0.448	0.566	21.03	0.486	0.565	24.06	0.496
CityGaussian	0.813	22.00	0.211	0.778	21.55	0.246	0.813	25.77	0.228
proposed	0.756	22.63	0.182	0.803	24.31	0.148	0.827	27.32	0.143

TABLE IV

A QUANTITATIVE COMPARISON WAS CONDUCTED ON THE WHU-OMVS DATASET. DUE TO THE LARGE SCALE OF THIS DATASET, 3D GAUSSIAN METHODS COULD NOT COMPLETE THE TRAINING, RESULTING IN OUT-OF-MEMORY (OOM) ERRORS. WE IMPLEMENTED SPECIFIC PARAMETER ADJUSTMENTS TO ENSURE THE METHOD COULD RUN PROPERLY.

method	PAG0.6m(%)	PAG0.8m(%)	PAG1.0m(%)	MAE(m)	RMSE(m)
w/o select and cull	69.16	75.69	79.65	0.701	1.449
proposed	81.29	86.13	88.78	0.467	1.019

TABLE V

ABLATION EXPERIMENTS ON THE WHU-OMVS DATASET, THE BEST RESULTS ARE HIGHLIGHTED IN BOLD.

method	PAG0.6m(%)	PAG0.8m(%)	PAG1.0m(%)	MAE(m)	RMSE(m)
w/o rgf	62.98	71.72	77.60	0.757	1.328
w/o mulgeo	74.28	79.43	82.36	0.654	1.446
proposed	81.29	86.13	88.78	0.467	1.019

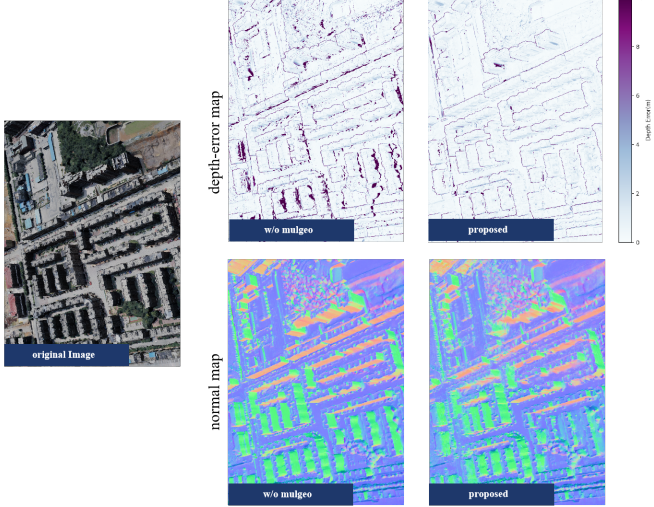


Fig. 8. Comparison with and without Multi-View Geometric Consistency. The comparison reveals that the proposed method, which includes multi-view geometric consistency, provides better detail recovery compared to the version without it.

and failure to ensure consistency across multiple viewpoints. To address this issue, we have introduced multi-view geometric consistency loss. Experiments in Table v demonstrate that the multi-view geometric consistency loss effectively enhances reconstruction accuracy. Disabling the loss results in a noticeable drop in accuracy, particularly in $PAG_{0.6}$ metric. Additionally, as can be seen from the error map of Fig.8, a significant increase in holes can be observed when multi-view geometric consistency is disabled.

VI. DISCUSSION

Application prospect: The proposed method matches the geometric accuracy of traditional open-source methods such as COLMAP and OpenMVS. However, there is still a gap compared to current deep learning-based MVS methods, particularly in the domain of photogrammetry, where further improvements in accuracy are necessary. However, a significant advantage of the 3DGS-based method over traditional MVS approaches lies in its ability to render high-fidelity images while reconstructing surfaces. This offers a new perspective for the field of surveying, allowing measurements to be derived not only from the reconstructed mesh but also from the high-resolution rendered images. Nonetheless, further research is needed to develop a suitable measurement method.

Resolution limitation: Aerial imagery typically has a resolution of 4K or higher. However, due to computational resource limitations, the 3DGS-based method cannot be trained directly on 4K images, necessitating downsampling. In [17] [13], the images were downsampled by a factor of four. In the field of surveying, high accuracy generally requires the use of original resolution images. This presents a significant barrier to applying 3DGS-based methods in the surveying field. In terms of future development direction, how to efficiently render high-resolution images is also a part that needs to be studied.

The SFM sparse point cloud limitation: The 3DGS-based method heavily relies on the sparse point cloud generated by SfM. In some datasets, which contain extensive textureless regions, present significant challenges due to the absence of initialized 3DGS primitives in these areas. The densification process attempts to address this by adding 3DGS primitives into the textureless regions. However, these primitives, guided solely by RGB image, do not accurately reflect the actual surface geometry. Due to the use of α -blending for image rendering, these primitives in textureless regions interfere with

the correct depth values of surrounding areas, leading to depth estimation errors. As a result, the proposed method performs suboptimally on datasets with extensive textureless regions. There remains considerable room for improvement in our approach. In the future, we could explore SfM techniques specifically designed for textureless regions or introduce constraints to enhance the performance of the 3DGS-based method in these areas.

VII. CONCLUSION

In this paper, we present AGS Gaussian, the first method to achieve large-scale surface geometry reconstruction from aerial imagery using a 3D Gaussian Splatting-based approach. The proposed method introduces a data chunking strategy specifically designed for aerial imagery, allowing each data block to be independently trained on multiple GPUs, with seamless stitching after training. We also incorporate Ray-Gaussian Intersection to enforce strong geometric constraints. Additionally, we integrate a multi-view geometric consistency loss to ensure geometric coherence across multiple views. We validated the geometric accuracy of our approach on the WHU-OMVS and assessed the rendering quality on the Mill-19 and UrbanScene3D datasets. The experimental results demonstrate that the proposed method effectively performs geometric surface reconstruction in large-scale scenes while achieving excellent rendering quality.

REFERENCES

- [1] Jonathan T Barron, Ben Mildenhall, Matthew Tancik, Peter Hedman, Ricardo Martin-Brualla, and Pratul P Srinivasan. Mip-nerf: A multiscale representation for anti-aliasing neural radiance fields. In *Proceedings of the IEEE/CVF international conference on computer vision*, pages 5855–5864, 2021.
- [2] Mehmet Buyukdemircioglu and Sultan Kocaman. Reconstruction and efficient visualization of heterogeneous 3d city models. *Remote Sensing*, 12(13):2128, 2020.
- [3] Nina Danilina, Mihail Slepnev, and Spartak Chebotarev. Smart city: Automatic reconstruction of 3d building models to support urban development and planning. In *MATEC Web of Conferences*, volume 251, page 03047. EDP Sciences, 2018.
- [4] Sara Fridovich-Keil, Alex Yu, Matthew Tancik, Qinhong Chen, Benjamin Recht, and Angjoo Kanazawa. Plenoxels: Radiance fields without neural networks. In *Proceedings of the IEEE/CVF conference on computer vision and pattern recognition*, pages 5501–5510, 2022.
- [5] Jiaming Gu, Minchao Jiang, Hongsheng Li, Xiaoyuan Lu, Guangming Zhu, Syed Afq Ali Shah, Liang Zhang, and Mohammed Bennamoun. Ue4-nerf: Neural radiance field for real-time rendering of large-scale scene. *Advances in Neural Information Processing Systems*, 36, 2024.
- [6] Antoine Guédon and Vincent Lepetit. Sugar: Surface-aligned gaussian splatting for efficient 3d mesh reconstruction and high-quality mesh rendering. In *Proceedings of the IEEE/CVF Conference on Computer Vision and Pattern Recognition*, pages 5354–5363, 2024.
- [7] Heiko Hirschmuller. Stereo processing by semiglobal matching and mutual information. *IEEE Transactions on pattern analysis and machine intelligence*, 30(2):328–341, 2007.
- [8] Wenbo Hu, Yuling Wang, Lin Ma, Bangbang Yang, Lin Gao, Xiao Liu, and Yuewen Ma. Tri-miprf: Tri-mip representation for efficient anti-aliasing neural radiance fields. In *Proceedings of the IEEE/CVF International Conference on Computer Vision*, pages 19774–19783, 2023.
- [9] Binbin Huang, Zehao Yu, Anpei Chen, Andreas Geiger, and Shenghua Gao. 2d gaussian splatting for geometrically accurate radiance fields. In *ACM SIGGRAPH 2024 Conference Papers*, pages 1–11, 2024.
- [10] Bernhard Kerbl, Georgios Kopanas, Thomas Leimkühler, and George Drettakis. 3d gaussian splatting for real-time radiance field rendering. *ACM Trans. Graph.*, 42(4):139–1, 2023.
- [11] Leonid Keselman and Martial Hebert. Approximate differentiable rendering with algebraic surfaces. In *European Conference on Computer Vision*, pages 596–614. Springer, 2022.
- [12] Zhaoshuo Li, Thomas Müller, Alex Evans, Russell H Taylor, Matthias Unterath, Ming-Yu Liu, and Chen-Hsuan Lin. Neuralangelo: High-fidelity neural surface reconstruction. In *Proceedings of the IEEE/CVF Conference on Computer Vision and Pattern Recognition*, pages 8456–8465, 2023.
- [13] Jiaqi Lin, Zhihao Li, Xiao Tang, Jianzhuang Liu, Shiyong Liu, Jiayue Liu, Yangdi Lu, Xiaofei Wu, Songcen Xu, Youliang Yan, et al. Vastgaussian: Vast 3d gaussians for large scene reconstruction. In *Proceedings of the IEEE/CVF Conference on Computer Vision and Pattern Recognition*, pages 5166–5175, 2024.
- [14] Liqiang Lin, Yilin Liu, Yue Hu, Xingguang Yan, Ke Xie, and Hui Huang. Capturing, reconstructing, and simulating: the urbanscene3d dataset. In *European Conference on Computer Vision*, pages 93–109. Springer, 2022.
- [15] Jin Liu, Jian Gao, Shunping Ji, Chang Zeng, Shaoyi Zhang, and JianYa Gong. Deep learning based multi-view stereo matching and 3d scene reconstruction from oblique aerial images. *ISPRS Journal of Photogrammetry and Remote Sensing*, 204:42–60, 2023.
- [16] Jin Liu and Shunping Ji. A novel recurrent encoder-decoder structure for large-scale multi-view stereo reconstruction from an open aerial dataset. In *Proceedings of the IEEE/CVF conference on computer vision and pattern recognition*, pages 6050–6059, 2020.
- [17] Yang Liu, He Guan, Chuanchen Luo, Lue Fan, Junran Peng, and Zhaoxiang Zhang. Citygaussian: Real-time high-quality large-scale scene rendering with gaussians. *arXiv preprint arXiv:2404.01133*, 2024.
- [18] Tao Lu, Mulin Yu, Linning Xu, Yuanbo Xiangli, Limin Wang, Dahua Lin, and Bo Dai. Scaffold-gs: Structured 3d gaussians for view-adaptive rendering. In *Proceedings of the IEEE/CVF Conference on Computer Vision and Pattern Recognition*, pages 20654–20664, 2024.
- [19] Li Ma, Xiaoyu Li, Jing Liao, Qi Zhang, Xuan Wang, Jue Wang, and Pedro V Sander. Deblur-nerf: Neural radiance fields from blurry images. In *Proceedings of the IEEE/CVF Conference on Computer Vision and Pattern Recognition*, pages 12861–12870, 2022.
- [20] Dominique Meyer, Elioth Fraijo, Eric Lo, Dominique Rissolo, and Falko Kuester. Optimizing uav systems for rapid survey and reconstruction of large scale cultural heritage sites. In *2015 Digital Heritage*, volume 1, pages 151–154. IEEE, 2015.
- [21] Ben Mildenhall, Pratul P Srinivasan, Matthew Tancik, Jonathan T Barron, Ravi Ramamoorthi, and Ren Ng. Nerf: Representing scenes as neural radiance fields for view synthesis. *Communications of the ACM*, 65(1):99–106, 2021.
- [22] Albert Pumarola, Enric Corona, Gerard Pons-Moll, and Francesc Moreno-Noguer. D-nerf: Neural radiance fields for dynamic scenes. In *Proceedings of the IEEE/CVF Conference on Computer Vision and Pattern Recognition*, pages 10318–10327, 2021.
- [23] Johannes Lutz Schönberger and Jan-Michael Frahm. Structure-from-motion revisited. In *Conference on Computer Vision and Pattern Recognition (CVPR)*, 2016.
- [24] Johannes Lutz Schönberger, Enliang Zheng, Marc Pollefeys, and Jan-Michael Frahm. Pixelwise view selection for unstructured multi-view stereo. In *European Conference on Computer Vision (ECCV)*, 2016.
- [25] Matthew Tancik, Vincent Casser, Xinchen Yan, Sabeek Pradhan, Ben Mildenhall, Pratul P Srinivasan, Jonathan T Barron, and Henrik Kretzschmar. Block-nerf: Scalable large scene neural view synthesis. In *Proceedings of the IEEE/CVF Conference on Computer Vision and Pattern Recognition*, pages 8248–8258, 2022.
- [26] Hāithem Turki, Deva Ramanan, and Mahadev Satyanarayanan. Meganerf: Scalable construction of large-scale nerfs for virtual fly-throughs. In *Proceedings of the IEEE/CVF Conference on Computer Vision and Pattern Recognition*, pages 12922–12931, 2022.
- [27] Peng Wang, Lingjie Liu, Yuan Liu, Christian Theobalt, Taku Komura, and Wenping Wang. Neus: Learning neural implicit surfaces by volume rendering for multi-view reconstruction. *arXiv preprint arXiv:2106.10689*, 2021.
- [28] Diana Werner, Ayoub Al-Hamadi, and Philipp Werner. Truncated signed distance function: experiments on voxel size. In *Image Analysis and Recognition: 11th International Conference, ICIAR 2014, Vilamoura, Portugal, October 22–24, 2014, Proceedings, Part II 11*, pages 357–364. Springer, 2014.
- [29] Linning Xu, Yuanbo Xiangli, Sida Peng, Xingang Pan, Nanxuan Zhao, Christian Theobalt, Bo Dai, and Dahua Lin. Grid-guided neural radiance fields for large urban scenes. In *Proceedings of the IEEE/CVF Conference on Computer Vision and Pattern Recognition*, pages 8296–8306, 2023.

- [30] Yao Yao, Zixin Luo, Shiwei Li, Tian Fang, and Long Quan. Mvsnet: Depth inference for unstructured multi-view stereo. In *Proceedings of the European conference on computer vision (ECCV)*, pages 767–783, 2018.
- [31] Zehao Yu, Anpei Chen, Binbin Huang, Torsten Sattler, and Andreas Geiger. Mip-splatting: Alias-free 3d gaussian splatting. In *Proceedings of the IEEE/CVF Conference on Computer Vision and Pattern Recognition*, pages 19447–19456, 2024.
- [32] Zehao Yu, Torsten Sattler, and Andreas Geiger. Gaussian opacity fields: Efficient and compact surface reconstruction in unbounded scenes. *arXiv preprint arXiv:2404.10772*, 2024.
- [33] MI Zhenxing and Dan Xu. Switch-nerf: Learning scene decomposition with mixture of experts for large-scale neural radiance fields. In *The Eleventh International Conference on Learning Representations*, 2022.